Lithium-Ion Batteries

International Edition: DOI: 10.1002/anie.201501475
German Edition: DOI: 10.1002/ange.201501475

Controllable Synthesis of Mesoporous Peapod-like Co_3O_4@Carbon Nanotube Arrays for High-Performance Lithium-Ion Batteries**

Dong Gu, Wei Li, Fei Wang, Hans Bongard, Bernd Spliethoff, Wolfgang Schmidt, Claudia Weidenthaler, Yongyao Xia, Dongyuan Zhao, and Ferdi Schüth**

Abstract: *Transition metal oxides are regarded as promising anode materials for lithium-ion batteries because of their high theoretical capacities compared with commercial graphite. Unfortunately, the implementation of such novel anodes is hampered by their large volume changes during the Li^+ insertion and extraction process and their low electric conductivities. Herein, we report a specifically designed anode architecture to overcome such problems, that is, mesoporous peapod-like Co_3O_4@carbon nanotube arrays, which are constructed through a controllable nanocasting process. Co_3O_4 nanoparticles are confined exclusively in the intratubular pores of the nanotube arrays. The pores between the nanotubes are open, and thus render the Co_3O_4 nanoparticles accessible for effective electrolyte diffusion. Moreover, the carbon nanotubes act as a conductive network. As a result, the peapod-like Co_3O_4@carbon nanotube electrode shows a high specific capacity, excellent rate capacity, and very good cycling performance.*

Lithium-ion batteries (LIBs) are widely used in consumer electronics, transportation, and large-scale renewable energy storage.[1] In particular, they are one type of the most popular rechargeable batteries for specific applications, such as in electric vehicles, locomotives, and for aerospace applications. However, energy densities and cycle lives of existing batteries are still quite limited and do not satisfy the challenging demands of future applications.[2] Thus, it is crucial to develop new and well-designed electrode materials with high performance. Co_3O_4 has attracted extensive interest for LIBs due to its high theoretical capacity of 890 $mAh\,g^{-1}$, which is more than two times higher than that of commercial graphite (372 $mAh\,g^{-1}$). Moreover, cobalt oxide is also quite abundant, has relatively low costs, and low toxicity. It is thus considered a promising candidate as an anode material of the next generation of LIBs. However, its large volume expansion/contraction and severe particle aggregation associated with the Li^+ insertion/extraction process normally lead to electrode pulverization and a loss of interparticle contact. Thus, substantial and irreversible capacity loss is observed during charge/discharge cycles.

In the past, substantial efforts have been directed toward mitigating the adverse mechanical effects and improving the overall electrochemical performance of Co_3O_4 anodes. One interesting strategy is to design unique Co_3O_4 nano-/microstructures, such as nanowires,[3] nanotubes,[4] octahedral cages,[5] nanoplates,[6] and hollow nanospheres.[7] These nanostructures can not only enable rapid Li^+ transport within the free volume around the nanoparticles, but also facilitate volume-strain relaxation. Another effective strategy is to construct Co_3O_4/carbon hybrid materials. Carbon usually does enhance the electrical conductivity within such hybrid materials. On the other hand, carbon coatings on Co_3O_4 nanostructures can help to accommodate the large volume changes during the charge/discharge process. Although numerous Co_3O_4/carbon hybrid nanostructures, such as carbon nanotube/Co_3O_4,[8] graphene/Co_3O_4,[9] and Co_3O_4@carbon composites,[10] have been created, and proven more or less effective for LIBs, there is still plenty of room for further improvement.[11] Mesoporous carbon materials have attracted intense interest as electrode materials for energy storage and conversion because of their high surface area, electrical conductivity, chemical stability, and low cost, especially as supports for well-dispersed active nanoparticles. At low metal content and/or low temperatures during preparation or use, the nanoparticles can be well dispersed and remain confined. However, at high metal loading or high temperatures, the metal species normally aggregate severely into larger particles. Moreover, the loaded nanoparticles do inevitably block the pore system of conventional mesoporous carbon to a certain extent. Therefore, loading of highly concentrated (e.g., >50 wt%) and well-dispersed crystalline nanoparticles into predefined mesopores of carbon without aggregation and blockage of the open pore system is still challenging.

Herein, we report a controllable nanocasting method for the spatial and size-selective synthesis of well-dispersed Co_3O_4 nanoparticles in mesoporous carbons with a high loading amount of up to 70 wt%. CMK-5, an ordered mesoporous carbon consisting of hexagonally packed carbon nanotubes (in the following abbreviated as CNT, but

[*] Dr. D. Gu,[+] H. Bongard, B. Spliethoff, Dr. W. Schmidt, Dr. C. Weidenthaler, Prof. Dr. F. Schüth
Max-Planck-Institut für Kohlenforschung
45470 Mülheim an der Ruhr (Germany)
E-mail: schueth@mpi-muelheim.mpg.de
Dr. W. Li,[+] F. Wang, Prof. Dr. Y. Y. Xia, Prof. Dr. D. Y. Zhao
Department of Chemistry, Laboratory of Advanced Materials
Shanghai Key Lab of Molecular Catalysis and Innovative Materials
and State Key Laboratory of Molecular Engineering of Polymers
Fudan University
Shanghai 200433 (P. R. China)
E-mail: dyzhao@fudan.edu.cn
[+] These authors contributed equally to this work.

[**] This work was supported by the Alexander von Humboldt-Stiftung and NSF of China (21210004), in addition to the basic support by the Max Planck Society.
Supporting information for this article is available on the WWW under http://dx.doi.org/10.1002/anie.201501475.

one should keep in mind that the local order of the carbon atoms in these tubes is lower than in typical single- or multiwalled CNTs),[12] has been used as an ideal substrate for such approaches. A gentle oxidation method with acidic ammonium persulfate (APS) as the oxidant is utilized to decorate the pore walls of the intratubular surface with a high concentration of oxygen-containing groups,[13] which facilitates local anchoring of Co_3O_4 nanoparticles in the pores. The obtained mesoporous peapod-like Co_3O_4@carbon nanotube arrays (Co_3O_4@CNT) have high surface areas of up to 750 $m^2 g^{-1}$ and large pore sizes. The particle sizes of Co_3O_4 can be controlled between 3–7 nm by varying the thickness of the carbon layer, and their loading amount can be varied from 45 to 70 wt%. Owing to the unique nanostructures, the resultant Co_3O_4@CNT material shows a high specific capacity of 780 mAh g^{-1} (the volumetric capacity is calculated to be about 1370 mAh cm^{-3}) at a current density of 100 mA g^{-1}, an excellent rate capacity, and cycling performance.

The synthesis process is illustrated in Figure 1. Detailed experimental steps are described in the Supporting Information. The mesostructure transformations during the synthesis process were monitored by low-angle X-ray diffraction (XRD; Figure S1). The parent SBA-15 hard template shows five well-resolved reflections, which can be indexed as the (100), (110), (200), (210), and (220) reflections in *p6mm* symmetry (Figure S1a), which is characteristic for the two-dimensional (2-D) hexagonal mesostructure.[14] Upon the surface casting with carbon and surface functionalization by APS, the resultant CNT@SBA-15 composites retain a highly ordered mesostructure (Figure S1b,c). This indicates a uniform coating of a carbon layer on the internal mesopore surfaces of SBA-15. The resultant CMK-5-type carbon shows five well-resolved reflections (Figure S1f), which is consistent with previous results,[12b] indicating that high quality nanotube arrays are formed. After deposition of Co_3O_4 nanoparticles into functionalized CNT@SBA-15, the as-obtained Co_3O_4@CNT@SBA-15 products still exhibit three reflections (Figure S1d). After removal of the silica scaffolds by aqueous NaOH solution, the mesoporous Co_3O_4@CNT products display only a broad signal with low intensity (Figure S1e). The fact that the reflections from the CMK-5 host are not visible can be explained by the low electron density of the carbon materials compared to that of Co_3O_4. The Co_3O_4 nanoparticles cause small-angle scattering of the X-rays and the scattering intensity of the nanoparticles is much higher than that for the CMK-5 matrix.

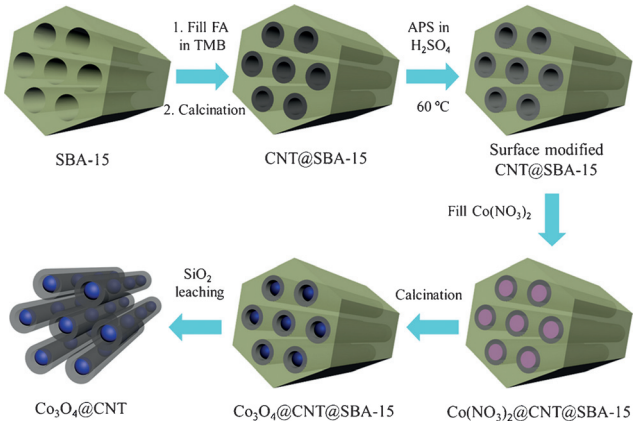

Figure 1. Schematic illustration of the formation process of the mesoporous peapod-like Co_3O_4@carbon nanotube arrays (Co_3O_4@CNT). TMB: 1,2,4-trimethylbenzene.

Scanning electron microscopy (SEM) images (Figure 2a) show that the Co_3O_4@CNT products have rod-like morphologies with a particle size of about 0.8–1.0 μm, analogous to the parent SBA-15 template. Almost no Co_3O_4 nanoparticles are observed on the external surface of the carbon matrix, indicating a perfect filling of Co_3O_4 nanoparticles in the mesopores of the CMK-5. To analyze the nanoparticle distribution in the carbon matrix, Co_3O_4@CNT samples were embedded in a resin and cut into microtomed slices for analysis with high-resolution SEM (HR-SEM). As shown in Figure 2b, Co_3O_4 nanoparticles (bright spots) are uniformly embedded in the tubular mesopores of the carbon matrix. The corresponding bright-field scanning transmission electron microscope (BF-STEM) image (Figure 2c) also shows that the Co_3O_4 nanoparticles (dark spots) are completely confined within the nanotubes. The image also shows the parallel alignment of the carbon nanotubes. Co elemental mapping (Figure S3) corroborates the inclusion of the Co_3O_4 nanoparticles inside the CNT channels. The TEM image (Figure 2d) further confirms that the Co_3O_4@CNT samples retain the same morphology and an ordered mesostructure as the parent SBA-15 template. As clearly demonstrated, Co_3O_4 nanoparticles are highly dispersed and homogeneously encapsulated in the mesopore channels with uniform sizes

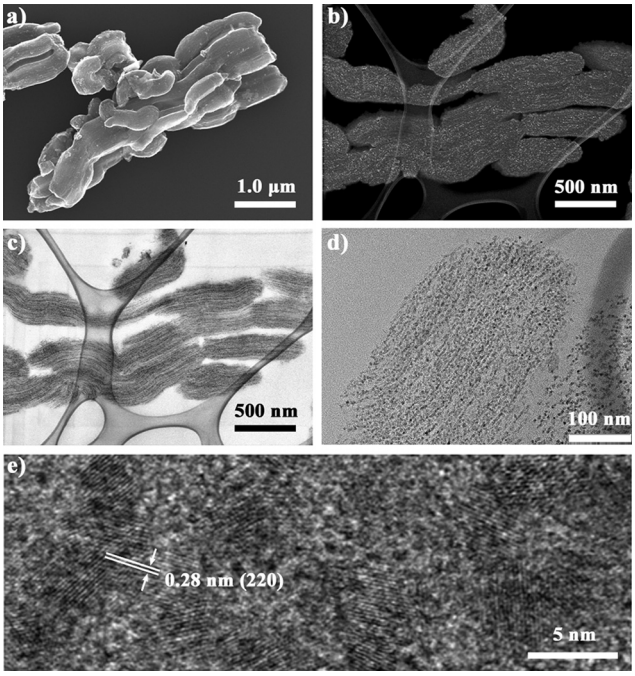

Figure 2. a) SEM images of the composite Co_3O_4@CNT-2. b) SEM, c) BF-STEM, d) TEM, and e) HR-TEM images of thin microtome sections of the composite Co_3O_4@CNT-2.

of 4–5 nm and distances of about 3 nm between adjacent nanoparticles. No bulky aggregates are visible. The particle sizes of Co_3O_4 are limited by the diameters of the tubular mesopores. However, also slightly elongated particles are observed due to growth along the channels. The confining effect of the mesopore channels is clearly visible.[15] The HR-TEM image (Figure 2e) shows that Co_3O_4 nanoparticles are highly crystalline, as indicated by well-defined lattice planes, which can be identified by their *d* spacing of 0.28 nm as the (220) crystal planes of spinel Co_3O_4. The wide-angle XRD pattern of Co_3O_4@CNT products (Figure S2) displays broad reflections, which can be well assigned to Co_3O_4 with $Fd\bar{3}m$ symmetry (PDF-2: 42-1467). Co_3O_4 nanoparticles are also detected in XPS spectra (Figure S4) which could be due to the presence of some particles on the surface and/or the thin carbon walls through which the electrons can still escape.

The wall thickness of the carbon nanotubes in the Co_3O_4@CNT products can be controlled by adjusting the initial loading amount of the carbon precursor in the SBA-15 template. N_2 sorption isotherms of the CNT@SBA-15 templates with different carbon contents all show typical type IV curves with more or less H1-type hysteresis loops (Figure S5A). With increasing amount of carbon precursor (from 25 to 75% pore volume filling with FA precursor, denoted as CNT@SBA-15-1, -2 and -3, respectively), the adsorption and desorption steps shift to lower relative pressures accompanied by a significant decrease of the mesopore volume, indicating that the pore system is gradually filled with carbon. The results of the sorption analyses are compiled in Table S1. Compared with the parent SBA-15, notable reductions of specific surface areas from about 793 to 383 $m^2 g^{-1}$ and pore volumes from 1.08 down to 0.38 $cm^3 g^{-1}$ are observed in CNT@SBA-15 templates (Table S1). The corresponding pore size distributions of the CNT@SBA-15 materials (Figure S5B) also show gradually decreasing pore diameters from 7.7 to 4.9 nm (Table S1). The wall thickness of these carbon nanotubes in the samples CNT@SBA-15-1, CNT@SBA-15-2, and CNT@SBA-15-3 were estimated to be about 0.60, 1.05, and 1.40 nm, respectively (Table S1).

Figure 3 shows the TEM images of Co_3O_4@CNT products templated from CNT@SBA-15-1, CNT@SBA-15-2, and CNT@SBA-15-3, respectively. It was found that the density of Co_3O_4 loading increases with the decrease of the nanotube wall thickness because of the gradually higher levels of loading of cobalt nitrate precursors resulting from the increased pore volume of the CNT@SBA-15 templates at lower carbon wall thickness (from 0.38 to 0.49 and 0.55 $cm^3 g^{-1}$ (Table S1)). Notably, large-domain TEM and BF-STEM images show that almost all of the Co_3O_4 nanoparticles are well encapsulated within the carbon matrix (Figure S6), again proving the confinement effect of the carbon matrix. The different carbon materials show also well-preserved structures after leaching of the silica template. The size of Co_3O_4 nanoparticles decreases from about 7 to 5 and 3 nm, which is consistent with the XRD results (the width of the reflections increases as the internal diameters of CNTs decrease; Figure S2). Co_3O_4 contents in Co_3O_4@CNT-1, Co_3O_4@CNT-2, and Co_3O_4@CNT-3 products were determined by thermogravimetric analyses (TGA) to be 70.2, 57.3, and 46.7 wt%,

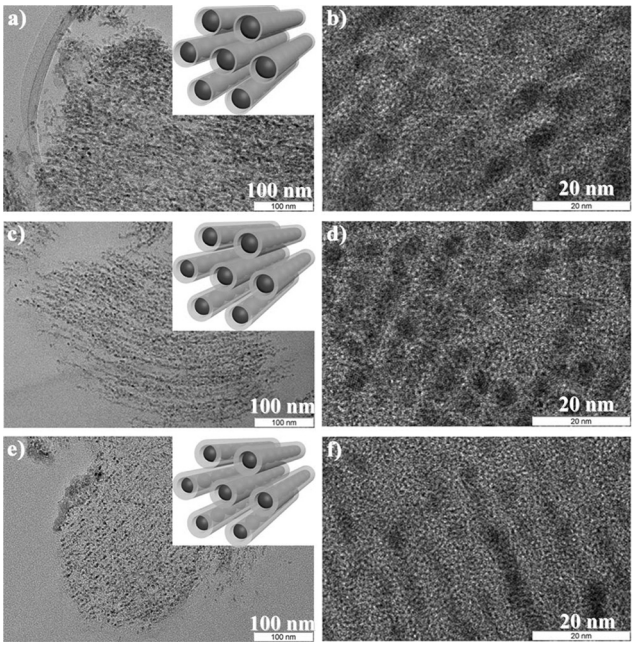

Figure 3. TEM images of thin microtome sections of a,b) Co_3O_4@CNT-1, c,d) Co_3O_4@CNT-2, and e,f) Co_3O_4@CNT-3. The insets in (a), (c), and (e) are the corresponding schematic images.

respectively (Figure S7). N_2 sorption isotherms of Co_3O_4@CNT products show that the resultant materials are still mesoporous (Figure S8A). Compared with the CMK-5 carbon (1818 $m^2 g^{-1}$ and 1.81 $cm^3 g^{-1}$, Figure S9), the BET surface areas of Co_3O_4@CNT products are greatly decreased from about 748 down to 293 $m^2 g^{-1}$, and the pore volumes are decreased from 0.50 down to 0.29 $cm^3 g^{-1}$. These numbers are quite high. The corresponding pore size distributions (Figure S8B) show a monomodal pore system in the mesopore range, resulting from the silica leaching. The intratubular pores of CMK-5 are possibly partly blocked for gas adsorption by Co_3O_4 nanoparticles, and partly so narrow, due to the cobalt oxide particles, that nitrogen is adsorbed in the pressure range characteristic for adsorption in micropores.

Thus, we have demonstrated that CMK-5 offers a flexible mesoporous platform for spatial and size selective loading of nanoparticles, because the intratubular pores and the pores between the carbon tubes are formed separately. The functionalization of the carbon surface plays a very important role in the formation of the unique peapod-like Co_3O_4@CNT structure, especially at high loadings. Firstly, the surface oxygen-containing groups increase the hydrophilicity of the carbon nanotube's inner surface, allowing for an effective infiltration of the cobalt precursor. Secondly, the oxygen-containing functional groups on the carbon surface could act as ion exchangers. The cobalt ions are effectively attached to the carbon surface, and cobalt carbonate species can be formed, which may locally chelate cobalt species on the carbon surface. Therefore, the cobalt species cannot easily migrate within the mesopore channels during the successive decomposition process, and only Co_3O_4 nanoparticles with uniform peapod morphology are formed locally in the carbon channels.[16]

The electrochemical performance of the Co_3O_4@CNT samples as anode materials for LIBs was investigated by galvanostatic charge/discharge measurements over a voltage range of 0–3.0 V, taking the sample Co_3O_4@CNT-1 as an example. For comparison, ordered mesoporous Co_3O_4 was synthesized from SBA-15 by the same nanocasting method, but without carbon coating.[17] The TEM image (Figure S10) shows that the as-obtained mesoporous Co_3O_4 possesses a highly ordered mesostructure, consisting of uniform nanowire arrays. The material has a BET surface area of 85 $m^2 g^{-1}$ and a mesopore size of 3.4 nm (Figure S11). Figure 4a shows

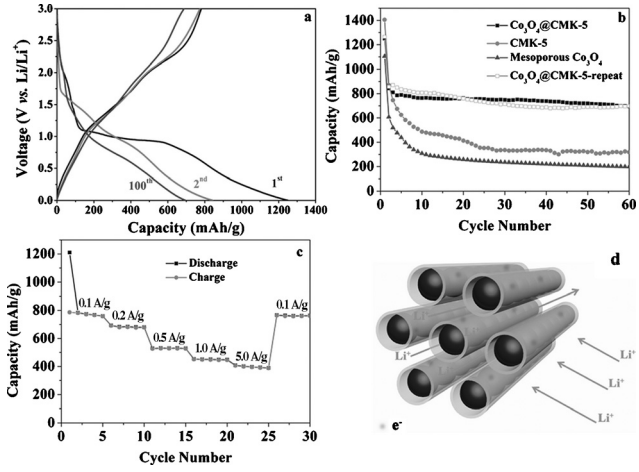

Figure 4. a) Charge/discharge curves of the Co_3O_4@CNT-1 electrode at a current density of 0.1 $A g^{-1}$. b) Cycling performance of the Co_3O_4@CNT-1, CMK-5, and mesoporous Co_3O_4 electrodes at constant current densities of 0.1 $A g^{-1}$. c) Cycling performance of the Co_3O_4@CNT-1 electrode at different current densities from 0.1 to 5.0 $A g^{-1}$. All measurements were conducted within a voltage window of 0–3.0 V. d) Schematic representation of the electrochemical reaction path on the Co_3O_4@CNT electrode materials.

typical charge/discharge curves of a Co_3O_4@CNT electrode at a current density of 0.1 $A g^{-1}$, which clearly exhibits two distinct domains with a long voltage plateau at 1.03 V and a sloping curve down to the cutoff voltage of 0.01 V, indicative of the typical characteristics of Co_3O_4 electrodes. The mesoporous Co_3O_4 electrode shows a similar charge/discharge curve with a relatively short slope (Figure S12a). The short slope corresponds to the high surface area and small crystallite size of the Co_3O_4 nanocrystals in the Co_3O_4@CNT and mesoporous Co_3O_4 electrodes. However, no obvious voltage plateau is observed for CMK-5 carbon (Figure S12b), which is in agreement with previous reports. The apparent long slope results from the high surface area of CMK-5 which provides a large solid electrolyte interphase (SEI). The initial capacity loss may result from the incomplete conversion reaction and irreversible lithium loss due to the formation of the SEI layer. Notably, the Co_3O_4@CNT exhibits a much better cycling performance than CMK-5 and mesoporous Co_3O_4 at constant current density of 0.1 $A g^{-1}$ (Figure 4b). It can be seen that the reversible capacity of mesoporous Co_3O_4 fades rapidly from 607 to 199 mAh g^{-1} within 60 cycles. This is ascribed to the pulverization of Co_3O_4 nanoparticles in the absence of the carbon confinement. CMK-5 carbon is relatively stable but has only a relatively low remaining capacity of 318 mAh g^{-1} after 60 cycles (36.5% of the initial reversible capacity). In contrast, the Co_3O_4@CNT electrode maintains a high capacity of 700 mAh g^{-1} (based on the total mass of composite) and a Coulombic efficiency approaching almost 100% over 100 cycles (Figure S13). Considering the 29.8 wt% carbon in the Co_3O_4@CNT sample, one can estimate a capacity of 862 mAh g^{-1} contributed by Co_3O_4 in that cycle. This number is close to its theoretical capacity (890 mAh g^{-1}). Obviously, a strong synergistic effect exists between Co_3O_4 nanoparticles and CMK-5 carbon in the composite. This effect becomes more evident with cycling and probably plays a central role in the charge/discharge cycles in which it results in excellent cycling performance of the Co_3O_4@CNT. Reproduction of the experiments shows high reproducibility. The curve for the reproduced sample with a Co_3O_4 loading of 70 wt% is included in Figure 4b for comparison.

The rate capabilities of the Co_3O_4@CNT electrode were also evaluated by charge/discharge experiments at various current densities, ranging from 0.1 to 5.0 $A g^{-1}$ (Figure 4c). The Co_3O_4@CNT electrode clearly shows excellent cyclic capacity retention at each current density. Remarkably, high reversible capacities of about 453 and 408 mAh g^{-1} at current densities of 1.0 and 5.0 $A g^{-1}$ are still obtained, which correspond to 57.8 and 52.1% of the initial reversible capacity. These numbers are remarkably high compared to those reported previously for Co_3O_4/carbon hybrid materials (Table S2). Importantly, after high-current density measurements, the capacity of the Co_3O_4@CNT electrode at 0.1 $A g^{-1}$ can recover to its initial value, indicating a high reversibility of the system. The high performance of the Co_3O_4@CNT electrode can be explained as follows: 1) The carbon nanotubes can not only prevent the aggregation of Co_3O_4 nanoparticles and the cracking or crumbling of electrode materials during cycling (Figure S14), but also act as the conductive substrates for electron transport (Figure S15), which decreases the inner resistance of LIBs, therefore leading to a high specific capacity (Figure 4d, S16). 2) The spaces between the Co_3O_4 nanoparticles, originating from the transformation reaction, and the carbon nanotubes provide an elastic buffer space to allow volume expansion/contraction of Co_3O_4 nanoparticles during Li^+ insertion/extraction. Thus, large capacity, good Coulombic efficiency, and cycling stability are retained (Figure S16). 3) Due to the confinement effect of the carbon nanotubes, the Co_3O_4 nanoparticles have small particle sizes, which can increase the specific interfacial surface areas between electrolyte and active materials when recharged, and which is also favorable for lithium diffusion over Co_3O_4 nanoparticles (Figure 4d, S16).[18] 4) The open mesopores resulted from the removal of the silica do not only offer a high surface area for interfacial lithium storage, but also promote the electrolyte transport through the electrodes, which is responsible for the high rate capability and cycling stability (Figure 4d, S16).

In summary, mesoporous peapod-like Co_3O_4@carbon nanotube arrays have been rationally designed and fabricated by a controllable nanocasting method. The obtained meso-

porous Co_3O_4@CNT nanocomposites have a high surface area of up to 750 $m^2 g^{-1}$ and large pore size. The Co_3O_4 nanoparticles are exclusively confined and uniformly distributed in the intratubular mesopores of the mesoporous carbon nanotube arrays (CMK-5), whereas the pores between nanotubes remain open. The size of the Co_3O_4 nanoparticles can be controlled in the range of 3–7 nm by varying the thickness of the carbon layer, and the amount can be varied from 45 to 70 wt%. The unique structure of this material significantly promotes the accessibility of the Co_3O_4 nanoparticles as well as facilitates fast diffusional transport of guest ions. The Co_3O_4@CNT materials exhibit high specific capacity of up to 781 mAh g^{-1} (the Co_3O_4 contribution close to the theoretical capacity) at a current density of 100 mA g^{-1}, excellent rate capacity, and cycling performance. The performance of these products is superior to conventional mesoporous Co_3O_4 or pure CMK-5 carbon when used as anode materials for LIBs. More importantly, our approach can be easily extended to the synthesis of other mesoporous peapod-like metal oxide@CNT materials, which offers a new and general pathway for the rational design of functional materials for catalysis and energy storage or conversion.

Keywords: Co_3O_4/carbon nanocomposite · lithium ion batteries · mesoporous materials · template syntheses

How to cite: *Angew. Chem. Int. Ed.* **2015**, *54*, 7060–7064
Angew. Chem. **2015**, *127*, 7166–7170

[1] a) B. Kang, G. Ceder, *Nature* **2009**, *458*, 190; b) M. Armand, J. M. Tarascon, *Nature* **2008**, *451*, 652; c) P. G. Bruce, B. Scrosati, J.-M. Tarascon, *Angew. Chem. Int. Ed.* **2008**, *47*, 2930; *Angew. Chem.* **2008**, *120*, 2972; d) W. Li, F. Wang, S. S. Feng, J. X. Wang, Z. K. Sun, B. Li, Y. H. Li, J. P. Yang, A. A. Elzatahry, Y. Y. Xia, D. Y. Zhao, *J. Am. Chem. Soc.* **2013**, *135*, 18300.

[2] a) C. B. Zhu, X. K. Mu, P. A. van Aken, Y. Yu, J. Maier, *Angew. Chem. Int. Ed.* **2014**, *53*, 2152; *Angew. Chem.* **2014**, *126*, 2184; b) Z. Y. Wang, L. Zhou, X. W. Lou, *Adv. Mater.* **2012**, *24*, 1903; c) W. Wei, S. B. Yang, H. X. Zhou, I. Lieberwirth, X. L. Feng, K. Müllen, *Adv. Mater.* **2013**, *25*, 2909; d) L. W. Ji, Z. Lin, M. Alcoutlabi, X. W. Zhang, *Energy Environ. Sci.* **2011**, *4*, 2682; e) B. C. Melot, J. M. Tarascon, *Acc. Chem. Res.* **2013**, *46*, 1226; f) H. Liu, S. Chen, G. X. Wang, S. Z. Qiao, *Chem. Eur. J.* **2013**, *19*, 16897.

[3] a) K. M. Shaju, F. Jiao, A. Debart, P. G. Bruce, *Phys. Chem. Chem. Phys.* **2007**, *9*, 1837; b) Y. G. Li, B. Tan, Y. Y. Wu, *Nano Lett.* **2008**, *8*, 265; c) X. W. Lou, D. Deng, J. Y. Lee, L. A. Archer, *J. Mater. Chem.* **2008**, *18*, 4397.

[4] a) W. Y. Li, L. N. Xu, J. Chen, *Adv. Funct. Mater.* **2005**, *15*, 851; b) X. W. Lou, D. Deng, J. Y. Lee, J. Feng, L. A. Archer, *Adv. Mater.* **2008**, *20*, 258.

[5] X. Wang, L. J. Yu, X.-L. Wu, F. L. Yuan, Y.-G. Guo, Y. Ma, J. N. Yao, *J. Phys. Chem. C* **2009**, *113*, 15553.

[6] a) F. M. Zhan, B. Y. Geng, Y. J. Guo, *Chem. Eur. J.* **2009**, *15*, 6169; b) J. S. Chen, T. Zhu, Q. H. Hu, J. J. Gao, F. B. Su, S. Z. Qiao, X. W. Lou, *ACS Appl. Mater. Interfaces* **2010**, *2*, 3628.

[7] a) X. Wang, X. L. Wu, Y. G. Guo, Y. T. Zhong, X. Q. Cao, Y. Ma, J. N. Yao, *Adv. Funct. Mater.* **2010**, *20*, 1680; b) J. Y. Wang, N. L. Yang, H. J. Tang, Z. H. Dong, Q. Jin, M. Yang, D. Kisailus, H. J. Zhao, Z. R. Tang, D. Wang, *Angew. Chem. Int. Ed.* **2013**, *52*, 6417; *Angew. Chem.* **2013**, *125*, 6545.

[8] a) N. Du, H. Zhang, B. Chen, J. B. Wu, X. Y. Ma, Z. H. Liu, Y. Q. Zhang, D. Yang, X. H. Huang, J. P. Tu, *Adv. Mater.* **2007**, *19*, 4505; b) X. He, Y. Wu, F. Zhao, J. Wang, K. Jiang, S. Fan, *J. Mater. Chem. A* **2013**, *1*, 11121; c) M. Xu, F. Wang, Y. Zhang, S. Yang, M. Zhao, X. Song, *Nanoscale* **2013**, *5*, 8067; d) L. H. Zhuo, Y. Q. Wu, J. Ming, L. Y. Wang, Y. C. Yu, X. B. Zhang, F. Y. Zhao, *J. Mater. Chem. A* **2013**, *1*, 1141.

[9] a) Z. S. Wu, W. C. Ren, L. Wen, L. B. Gao, J. P. Zhao, Z. P. Chen, G. M. Zhou, F. Li, H. M. Cheng, *ACS Nano* **2010**, *4*, 3187; b) H. Kim, D. H. Seo, S. W. Kim, J. Kim, K. Kang, *Carbon* **2011**, *49*, 326.

[10] a) S. L. Xiong, J. S. Chen, X. W. Lou, H. C. Zeng, *Adv. Funct. Mater.* **2012**, *22*, 861; b) Y. Wang, H. J. Zhang, L. Lu, L. P. Stubbs, C. C. Wong, J. Y. Lin, *ACS Nano* **2010**, *4*, 4753; c) L. J. Zhi, Y.-S. Hu, B. E. Hamaoui, X. Wang, I. Lieberwirth, U. Kolb, J. Maier, K. Müllen, *Adv. Mater.* **2008**, *20*, 1727; d) F. B. Hao, Z. W. Zhang, L. W. Yin, *ACS Appl. Mater. Interfaces* **2013**, *5*, 8337; e) L. M. Wang, B. Liu, S. H. Ran, H. T. Huang, X. F. Wang, B. Liang, D. Chen, G. Z. Shen, *J. Mater. Chem.* **2012**, *22*, 23541; f) Y. T. Zhong, X. Wang, K. C. Jiang, J. Y. Zheng, Y. G. Guo, Y. Ma, J. N. Yao, *J. Mater. Chem.* **2011**, *21*, 17998.

[11] S. B. Yang, X. L. Feng, S. Ivanovici, K. Müllen, *Angew. Chem. Int. Ed.* **2010**, *49*, 8408; *Angew. Chem.* **2010**, *122*, 8586.

[12] a) S. H. Joo, S. J. Choi, I. Oh, J. Kwak, Z. Liu, O. Terasaki, R. Ryoo, *Nature* **2001**, *412*, 169; b) A.-H. Lu, W.-C. Li, W. Schmidt, W. Kiefer, F. Schüth, *Carbon* **2004**, *42*, 2939.

[13] a) Z. X. Wu, P. A. Webley, D. Y. Zhao, *Langmuir* **2010**, *26*, 10277; b) Z. X. Wu, W. Li, P. A. Webley, D. Y. Zhao, *Adv. Mater.* **2012**, *24*, 485.

[14] D. Y. Zhao, J. L. Feng, Q. S. Huo, N. Melosh, G. H. Fredrickson, B. F. Chmelka, G. D. Stucky, *Science* **1998**, *279*, 548.

[15] A.-H. Lu, J.-J. Nitz, M. Comotti, C. Weidenthaler, K. Schlichte, C. W. Lehmann, O. Terasaki, F. Schüth, *J. Am. Chem. Soc.* **2010**, *132*, 14152.

[16] a) X. H. Sun, Y. F. Shi, P. Zhang, C. M. Zheng, X. Y. Zheng, F. Zhang, Y. C. Zhang, N. J. Guan, D. Y. Zhao, G. D. Stucky, *J. Am. Chem. Soc.* **2011**, *133*, 14542; b) W. B. Yue, A. H. Hill, A. Harrison, W. Z. Zhou, *Chem. Commun.* **2007**, 2518; c) W. B. Yue, W. Z. Zhou, *Chem. Mater.* **2007**, *19*, 2359.

[17] D. Gu, F. Schüth, *Chem. Soc. Rev.* **2014**, *43*, 313.

[18] S. J. Ding, Z. Y. Wang, S. Madhavi, X. W. Lou, *J. Mater. Chem.* **2011**, *21*, 13860.

Received: February 17, 2015
Published online: April 27, 2015

